

Cite this: *Lab Chip*, 2016, **16**, 679

## On-chip preparation of nanoscale contrast agents towards high-resolution ultrasound imaging†

Sally A. Peyman,<sup>a</sup> James R. McLaughlan,<sup>b</sup> Radwa H. Abou-Saleh,<sup>ad</sup> Gemma Marston,<sup>c</sup> Benjamin R. G. Johnson,<sup>a</sup> Steven Freear,<sup>b</sup> P. Louise Coletta,<sup>c</sup> Alexander F. Markham<sup>c</sup> and Stephen D. Evans<sup>as</sup>

Micron-sized lipid-stabilised bubbles of heavy gas have been utilised as contrast agents for diagnostic ultrasound (US) imaging for many years. Typically bubbles between 1 and 8  $\mu\text{m}$  in diameter are produced to enhance imaging in US by scattering sound waves more efficiently than surrounding tissue. A potential area of interest for Contrast Enhanced Ultrasound (CEUS) are bubbles with diameters  $<1\text{ }\mu\text{m}$  or 'nanobubbles.' As bubble diameter decreases, ultrasonic resonant frequency increases, which could lead to an improvement in resolution for high-frequency imaging applications when using nanobubbles. In addition, current US contrast agents are limited by their size to the vasculature *in vivo*. However, molecular-targeted nanobubbles could penetrate into the extra-vascular space of cancerous tissue providing contrast in regions inaccessible to traditional microbubbles. This paper reports a new microfluidic method for the generation of sub-micron sized lipid stabilised particles containing perfluorocarbon (PFC). The nanoparticles are produced in a unique atomisation-like flow regime at high production rates, in excess of  $10^6$  particles per s and at high concentration, typically  $>10^{11}$  particles per mL. The average particle diameter appears to be around 100–200 nm. These particles, suspected of being a mix of liquid and gaseous  $\text{C}_4\text{F}_{10}$  due to Laplace pressure, then phase convert into nanometer sized bubbles on the application of US. *In vitro* ultrasound characterisation from these nanoparticle populations showed strong backscattering compared to aqueous filled liposomes of a similar size. The nanoparticles were stable upon injection and gave excellent contrast enhancement when used for *in vivo* imaging, compared to microbubbles with an equivalent shell composition.

Received 13th November 2015,  
Accepted 15th December 2015

DOI: 10.1039/c5lc01394a

[www.rsc.org/loc](http://www.rsc.org/loc)

### Introduction

Microbubbles (MBs) have been widely employed as ultrasound (US) contrast agents in medical imaging.<sup>1</sup> They typically contain a heavy gas core, such as a perfluorocarbon

(PFC) gas, and a lipid,<sup>2</sup> protein, or polymer shell and are between 1 and 8  $\mu\text{m}$  in diameter (Fig. 1).<sup>3</sup> Microbubbles provide contrast in US imaging by scattering ultrasound waves more efficiently than the surrounding tissue and recently there has been much interest in developing molecular-targeted microbubbles<sup>4</sup> and in using them as devices to enhance therapeutic delivery and uptake.<sup>5,6</sup> When the drug to be delivered is physically attached to the MB they are known as theranostic agents.<sup>7</sup>

An emerging area of interest is that of sub-micron bubbles. Nanobubbles, also defined as 'ultra-fine bubbles (50 nm–1  $\mu\text{m}$ ) have been the subject of much interest recently due to their potential for widespread commercial application in a diverse range of fields; from 'eco-cleaning' for removing dirt, salt, *etc.* from surfaces without the use of surfactants,<sup>5</sup> in the microfabrication industry for the floatation separation of semiconductor water treatment through to agriculture and plant irrigation.<sup>8–10</sup> The nanobubbles are generally formed *via* a gas nozzle submerged in water creating a high velocity jet<sup>6–8</sup> and are purported to be stable for prolonged periods, from weeks up to several months, even in the absence of surfactant coatings.<sup>10,11</sup> As the Laplace

<sup>a</sup> School of Physics and Astronomy, University of Leeds, LS2 9JT, UK

E-mail: s.d.evans@leeds.ac.uk

<sup>b</sup> School of Electronic and Electrical Engineering, University of Leeds, LS2 9JT, UK

<sup>c</sup> Leeds Institute for Molecular Medicine, St James's Hospital, Leeds, LS9 7TF, UK

<sup>d</sup> Department of Physics, Faculty of Science, Mansoura University, Egypt

† Electronic supplementary information (ESI) available: Supporting information S1: video of a bubble sample in a viewing chamber showing microbubbles rising to the top and underneath a population of smaller bubbles moving with Brownian motion. Supporting information S2: high speed imaging of the micro-spray regime (100 000 000 fps) showing the velocity of the microspray was still too high to capture single bubble formation. Supporting information S3: effect of lipid concentration on microspray particle size and concentration. S4: expansion ratio model used to calculate the predicted increase in nanoparticle diameter on the increase of temperature in Fig. 4a from ref. 42. Supporting information S5: comparison of lipid solution only passing through tubes of the set-up compared to lipid solution going through the microfluidic device. S6: plot to show change in resonant frequency *vs.* bubble diameter. S7: time *vs.* intensity curves to support *in vivo* observations in Fig. 7, TIC curves for microbubble only and nanobubble only. See DOI: 10.1039/c5lc01394a



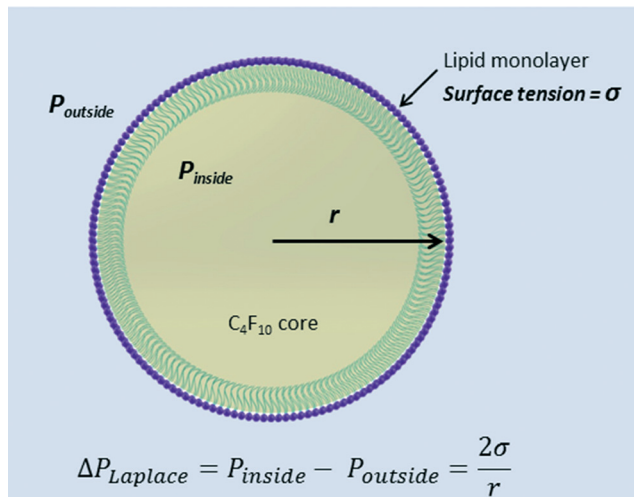


Fig. 1 Lipid stabilised nanoparticles in aqueous solution showing lipid monolayer shell. The  $C_4F_{10}$  may exist as a liquid core or a gas core depending on the size of the nanoparticle ( $r$ ) and the surface tension ( $\sigma$ ) (not to scale).

pressure is inversely proportional to the diameter of a bubble one would expect that the pressure inside the bubbles would be too great for them to exist for longer than a few microseconds.<sup>12</sup> There have been some conflicting theories as to the origin of the stability of such nanometer sized bubbles of gas in water ranging from; a lack of buoyancy, and an associated reduction in coalescence with the liquid–air interface at the top of a vial<sup>8</sup> to changes in the structure of the water at the nanobubble–gas interface. Ohgaki *et al.*, used ATR-IR to study the water–air interface and suggested that ‘hard’ hydrogen bonds similar to those found in ice promoted nanobubble longevity by containing the high internal pressures of the nanobubble and limit the diffusivity of gas out of the bubble and into the surrounding solution.<sup>11</sup>

Several groups have investigated the applicability of nanobubbles for Contrast Enhanced Ultrasound (CEUS). Xing *et al.* found that 400–600 nm diameter nanobubbles, produced by sonication, provided enhancement in *in vivo* US imaging.<sup>13</sup> Further, nanobubbles produced by mechanical agitation methods have been reported to display superior performance characteristics *in vivo* when compared to commercially available microbubbles in terms of contrast intensity and longevity.<sup>14,15</sup> The use of nanobubbles as drug delivery vehicles has also been investigated.<sup>16</sup> Zhang *et al.* who reported that nanobubbles formed by sonication, could be used as drug carriers for the treatment of residual tumour cells during High Frequency Ultrasound (HIFU) ablation. Nanobubbles loaded with methotrexate were described as a synergistic therapy, delivering the anti-cancer drug during the HIFU therapy to improve overall efficiency of tumour ablation.<sup>17</sup> Cavalli *et al.* demonstrated nanobubbles formed using an homogeniser as carrier agents for US mediated gene delivery.<sup>18</sup>

Nanobubbles have potential advantages over their micron-sized counterparts due to their ability to perfuse into

tumours, through ‘nanopores’ found in tumour blood vessels. These pores are of the order of 380–780 nm in diameter depending on the type of tumour.<sup>14,19</sup> This uptake of nanometer sized material, known as the enhanced permeability and retention or the EPR effect, could also improve drug delivery using nanobubbles by allowing deeper penetration of the delivery vehicle into the tumour. The Lapotko group have investigated another interesting potential application of nanobubbles in the clinic – the plasmonic nanobubble. Nanobubbles are generated by heating gold nanoparticles with a laser pulse. The group demonstrated that nanobubbles of controlled size could be produced by tuning the energy of laser and used for detection of cancerous cells or the selective destruction of the cell with mechanical ablation.<sup>20</sup> In a different example the nanoparticle–nanobubble technology was used for drug delivery by encapsulating nanoparticles and drugs inside a liposome. Nanoparticles were then overheated, producing nanobubbles which caused disruption of the liposome membrane and ejection of the drug payload.<sup>21</sup>

The preparation method of nanobubbles varies depending on the application. Industrial scale nanobubble preparation involves large volumes and high energy requirements, which has been suggested will limit their widespread use.<sup>8</sup> In his review, Zimmerman concluded that if energy efficient nanobubbles could be made, there would be widespread uptake of the technology.<sup>8</sup> Nanobubble fabrication techniques for medical applications have employed either sonication or mechanical agitation methods coupled with several labour intensive steps to attach drug or gene payloads to the nanobubble, depending on the biochemical complexity of the bubble shell.<sup>15–17,22</sup> Repeat handling of bubble samples can cause bubble loss through dilution or destruction and lower final bubble numbers.

Another, alternative method for producing microbubbles is the phase conversion of nano- or micro- meter sized low-boiling point PFC liquid droplets into PFC bubbles. The process, termed acoustic droplet vaporisation, is driven by pressures associated with an ultrasound wave.<sup>23</sup> Similarly an increase in temperature can also activate the droplets into bubbles by causing thermal expansion of the low-boiling point liquid. Phase-change contrast agents have shown excellent echogenicity during *in vitro*<sup>24,25</sup> and *in vivo* studies.<sup>26</sup> The nano- and micro- droplets generated for these applications are produced either by extrusion<sup>27</sup> or microbubble condensation, in which microbubbles are formed initially before being pressurised and slow-cooled to a liquid.<sup>24</sup>

A relatively new technology for the production of microbubbles is the use of microfluidics. There has been much work in recent years on the production of monodisperse micron sized bubbles for CEUS applications. Flow focussing microfluidic designs allows for greater control over the size of microbubbles produced and their polydispersity.<sup>28–30</sup> For example, Hettiarachchi and Talu *et al.* produced 1–5  $\mu$ m microbubbles with a dispersity index of <5%.<sup>31,32</sup> A similar approach for making uniformly sized phase-change contrast agents was described in which monodisperse microbubbles



where produced on-chip prior to bubble condensing into droplets.<sup>33</sup>

However, despite the elegant control over microbubble size, the above approaches suffer from low microbubble concentrations, which greatly limit their clinical applicability. We recently demonstrated that by introducing a sudden pressure drop, through expansion in outlet geometry of the chip that microbubbles could be produced in a 'microspray' regime, generating microbubbles at concentrations  $>10^9$  microbubbles per mL, a vast improvement on other microfluidic approaches. The microchip-microspray approach is simple to operate, highly reproducible and cheap to manufacture. The same design was also demonstrated for the rapid, single-step functionalisation of microbubbles with a therapeutic payload for targeted drug delivery.<sup>2,34</sup>

In this paper, we show that this same microchip and microspray regime leads to the facile production of high concentrations of nano-sized lipid stabilised PFC particles,  $\sim 10^{11}$ – $10^{12}$  mL<sup>-1</sup>, which dependent on their composition, size and surface tension exist in either their gaseous or liquid phase. For simplicity the mixed populations of nanobubbles and nanodroplets shall be referred to collectively as PFC 'nanoparticles.' Both nanodroplets and nanobubbles are thought to be acoustically active. Nanodroplets can undergo phase change into nanobubbles on application of temperature rise or a negative pressure US field.<sup>23</sup> In experiments where nanoparticles are exposed to ultrasound, they will be referred to as 'nanobubbles.' To our knowledge this is the first example of microfluidic production of high concentrations of nanoparticle phase change agents. The size and concentration of the nanoparticles produced by the microspray regime was characterised using a combination of complementary measurement techniques based on particle counting using a miniaturised coulter counter, dynamic light scattering (DLS) and particle tracking analysis. The response of the nanoparticles in an US field was also investigated both in a phantom, using a 15 MHz transducer, and in *in vivo* models, with a 40 MHz transducer. The nanoparticles showed superior contrast intensity *in vivo* when compared to the microbubbles samples, demonstrating their suitability as efficient contrast agents. Nanoparticles of PFC show the potential to improve spatial resolution for imaging using high frequency transducers (25–80 MHz), as used in pre-clinical imaging or in high frequency clinical US imaging applications.<sup>35,36</sup>

## Experimental

### Materials

Microbubbles and PFC nanoparticles were prepared from C<sub>4</sub>F<sub>10</sub> gas purchased from Air Liquide (Birmingham, UK), the surface coatings consisted of a lipid mixture (23.5  $\mu$ L DPPC at 20 mg mL<sup>-1</sup> and 3.5  $\mu$ L DSPE-PEG2000 at 25 mg mL<sup>-1</sup>) purchased from Avanti Polar Lipids (Alabaster, AL, USA). All lipids were dissolved in chloroform, dried on the wall of a glass vial under nitrogen for 40 minutes and then re-suspended in phosphate buffered saline (PBS, Sigma-Aldrich,

UK). The vial was then vortexed for 1 minute and placed in a heated ultrasonic bath for 1 hour to facilitate the re-suspension of the lipid mix.

### Microfluidic design and bubble generation

The microfluidic devices were fabricated by Epigem Ltd (Redcar, UK) in PMMA (polymethylmethacrylate) and SU-8. The microfluidic design had been described previously<sup>34</sup> but briefly, it consists of a central inlet channel for the gas and two opposing inlet channels for the introduction of the liquid phase. The flow was focussed through a nozzle beyond which there was a single exit channel. The chips were fabricated to a depth of 25  $\mu$ m, apart from the exit channel which had an additional 25  $\mu$ m depth, giving an overall depth of 50  $\mu$ m. The expanding 3D geometry was multiplexed to provide four bubble making geometries per chip to speed production. The chips were mounted in a custom-built holder on the moveable stage of an inverted light microscope (Eclipse Ti-U, Nikon, Japan). The chip holder consisted of a recess into which the microchip fitted closely. A manifold, which contained PTFE tubes (Supelco Analytical, USA) for liquid and gas lines was brought into firm contact with the chip using a lever clamping arm. In the closed position a gas tight seal between the manifold and chip was formed, even under high pressure conditions ( $>40$  psi). Fluid flow to the microchip was delivered *via* a Mitos P-Pump (Dolomite Ltd, UK) and the gas was regulated by a digital gas flow controller (Alicat Scientific, USA).

Microbubbles and nanoparticles were generated by pumping the aqueous lipid solution through opposing inlets and a gas flow through the central inlet (Fig. 2a). Liquid flow rate was 90  $\mu$ L mL<sup>-1</sup> and gas pressure set at 15 psi. A small delay, of a few seconds, was implemented before starting the bubble collection to ensure flow rates and gas pressures had reached their desired rate.

### Bubble separation and sizing

Microbubbles were separated from nanoparticles over time by a passive method that relies on the intrinsic buoyancy of the bubbles. A spherical bubble in a liquid medium has an ascension velocity,  $U$ , which can be calculated from the Hadamard-Rybczynski eqn (1).<sup>37</sup>

$$U = \frac{2gR^2\Delta\rho}{3\mu} \frac{\mu + \mu'}{2\mu + 3\mu'} \quad (1)$$

Where  $R$  is the radius,  $g$  is the gravitational acceleration (9.8 m s<sup>-2</sup>),  $\mu$  is the dynamic viscosity of water ( $8.90 \times 10^{-4}$  Pa s),  $\mu'$  is the dynamic viscosity of C<sub>4</sub>F<sub>10</sub> ( $1.2 \times 10^{-5}$  Pa s) and  $\Delta\rho$  is the difference in density between the medium and the gas core.<sup>37</sup> For a bubble with a 2  $\mu$ m diameter it would take 23 minutes to rise a distance of 1 cm. For a bubble with a diameter of 150 nm it would take 17 hours to travel the same distance. In the case of a nanodroplet with a diameter of



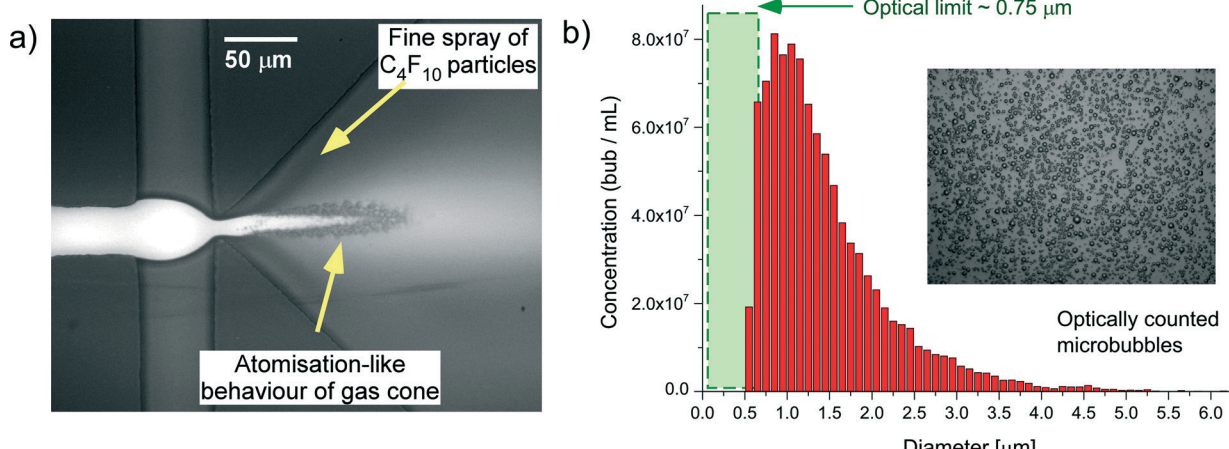


**Fig. 2** (a) Microspray bubble formation in a flow focussing microfluidic device featuring a 3D expanding geometry. (b) Histogram of bubble sizes when counted optically. Green shaded area indicates the optical limit ( $\sim 0.75 \mu\text{m}$ ) where nanoparticles are not resolved and counted. Insert shows a typical optical image of the microbubbles.

150 nm, and a density of  $1594 \text{ kg m}^{-3}$  it would sink by  $1.2 \mu\text{m}$  over the same time (23 min), and can be thought of as neutrally buoyant for these experiments. Based on this the bubble sample was left for  $\sim 45$  minutes to allow bubbles larger than  $1 \mu\text{m}$  to rise to the top of the vial, leaving behind the nanobubbles and neutrally buoyant nanodroplets. Nanobubbles and droplets do not scatter light as much as microbubbles and do not appear turbid to the eye. After 45 minutes the top layer of microbubbles was removed with a pipette and samples were taken from the lower, clear, portion of the vial. Sizing and counting of the separated samples was performed on a qNano (Izon, UK), *via* DLS (Zetasizer, Malvern Instruments, UK) and by a NanoSight instrument (Malvern Instruments, UK). For qNano measurements pore sizes of 100 nm up to 4000 nm were used to investigate the nanoparticle/bubble size ranges within the samples. Samples were diluted 1 in 100 prior to measurements. Microbubble samples were counted optically according to the methods published previously.<sup>34</sup>

### Ultrasound characterisation

Acoustic backscatter from bubble populations was measured using a focused 15 MHz single element ultrasound transducer (V313, Olympus KeyMed Ltd, Essex, UK) situated in a tank of degassed and filtered water. The ultrasound transducer was connected to a pulser/receiver (5072PR, Olympus KeyMed Ltd, Essex, UK), which generated a broadband ultrasound pulse that was scattered by the nanobubble/liposome populations. The populations were contained within a 100 mL cylindrical chamber that had acoustic windows to allow for interrogation of ultrasound, and were magnetically stirred to ensure a uniform distribution of particles. The backscattered signals were filtered (1 MHz high pass) and amplified by a 20 dB pre-amplifier built into the pulser/receiver unit. The filtered and amplified signal was digitised at a sampling frequency of 5 GHz using an 8 bit oscilloscope

(LeCroy 64Xi, LeCroy Corporation, Chestnut Ridge, NY) and downloaded to a PC. A total of 500 pulses were recorded at a pulse repetition frequency (PRF) of 0.5 kHz for each particle population, which were processed using Matlab (MathWorks Inc., Natick, MA). The received signal spectra were averaged in the frequency domain to reduce the variance of the experimental results due to external noise sources.<sup>38</sup> This process was repeated ( $n = 3$ ) for each population tested.

### *In vivo* imaging

Three CD1 nu/nu male mice age 6–8 weeks were imaged at 40 MHz with the VisualSonics Vevo770 High Frequency Ultrasound (HFUS). Mice were initially anaesthetised with 5% v/v isoflurane in medical air, which was then maintained at 3% during the imaging procedures. The aorta of the mouse was identified by an experienced HFUS user, with arterial flow confirmed with Pulsed Waved (PW) Doppler imaging. A 50 μL bolus of  $\sim 1 \times 10^9$  microbubbles per mL or  $10^{12}$  nanoparticle per mL sample (maximum gas volume fractions of  $4.2 \times 10^{-9} \text{ m}^3$  and  $1.8 \times 10^{-9} \text{ m}^3$ , respectively) was administered *via* a tail vein catheter at a rate of  $0.6 \text{ mL min}^{-1}$ , controlled *via* a syringe driver. Imaging was carried out under contrast B-mode, to acquire bubble wash-in curves for quantitative analysis with the wash in of bubbles. Data was analysed post acquisition with VisualSonics software to analyse time intensity wash-in curves and determination of  $I_{\min}$ ,  $I_{\max}$ , and flow rate.

Both *in vitro* and *in vivo* ultrasound systems were characterised using a calibrated 40 μm needle hydrophone (Precision Acoustics, Dorchester, UK). The *in vitro* system generated a 3-cycle pulse that had a peak positive pressure of  $3.90 \pm 0.08 \text{ MPa}$ , and a peak negative pressure of  $2.98 \pm 0.04 \text{ MPa}$ , which corresponded to a mechanical index (MI) of 0.74.<sup>39,40</sup> An A-line generated by the *in vivo* system consisted of a 2-cycle pulse, that in the focal region, had a free field peak positive pressure of  $2.6 \pm 0.15 \text{ MPa}$ , and a free field peak



negative pressure of  $2.89 \pm 0.02$  MPa, which corresponded to an MI of 0.49.

## Results and discussion

### Nanoparticle generation

Fig. 2a shows the microspray bubble formation regime generated in the 3D expanding geometry chips. The  $\text{C}_4\text{F}_{10}$  gas at a pressure of 15 psi ( $1.034 \times 10^5$  Pa) in the central channel is focused through the nozzle from inlet channels either side by a  $0.5 \text{ mg mL}^{-1}$  aqueous solution of lipids, typically at a flow rate of  $90 \mu\text{L min}^{-1}$ . As the gas and lipid solutions are pumped through the nozzle they experienced very high shear forces and velocity gradients. Immediately following the nozzle the 3D-expansion in the outlet caused a pressure drop in the outlet, inducing atomisation-like break-up of the gas cone and releasing bubbles in a fine spray. This atomisation-like behaviour produces a high concentration of microbubbles in the  $10^8$ – $10^9$  bubbles per mL with a size range between 1 and  $8 \mu\text{m}$ , when counted optically ( $\times 60$  optical magnification). The histograms of microbubble diameter, Fig. 2b, appear asymmetric; with a cut off for lower bubble size  $\sim 0.75 \mu\text{m}$  (the insert shows a brightfield image of the microbubbles). The lowest size on the histogram corresponds to the limit of the optical resolution of the  $60\times$  magnification used to count bubbles. In addition, optical images were taken at the upper surface of a flow cell, in which the bubbles have risen due to their intrinsic buoyancy. However, nano-sized particles such as nanodroplets and even nanobubbles, that are much smaller in size, remain homogenous in suspension due to Brownian motion. When the focus of the microscope was adjusted to go through a whole depth of the bubble sample, very tiny particles were observed moving with Brownian motion beneath the microbubble layer on top (see ESI† S1) suggesting there was a population of sub-micron particles produced during this regime that cannot be counted optically.

Fig. 2a shows an optical image taken of the microspray production at  $90\times$  magnification and the gas cone appears to show micron-sized bubbles breaking off the interface with the lipid solution. However, a finer spray of smaller particles can also be observed as a darker region very near to the nozzle.

Several papers have been published on the fluid mechanics behind high-pressure gas jets in liquid and the break up mechanisms that give rise to bubble production. Chen and Richter describe the process of bubbling and jetting in regimes under high gas pressures and turbulent flow.<sup>41</sup> The distinction between the two regimes depends on the linear velocity of the gas flow. Instances when the gas jet is sub-sonic (less than Mach 1) the gas cone breaks up into bubbles. When the velocity is supersonic (larger than Mach 0.9) then the gas cone moves into the jetting regime and breaks up some distance from the nozzle. In the case of the microspray regime, the linear velocity of the fluid can be easily calculated in the nozzle and equates to  $5 \text{ m s}^{-1}$ . This would give the

liquid alone a value of Mach 0.3. The Reynolds number inside the nozzle was calculated to be  $\sim 82$ , much higher than usually expected in microfluidic devices. However, this does not take into account the velocity of the gas jet, which cannot be measured using the current set-up. It may be that the linear velocity is even higher, pushing the Mach number up to unity.

A high-speed camera (SIMX16, Specialised Imaging, UK) was used to try to observe this phenomenon at a frame rate of  $\sim 1$  billion fps. However, the microspray break up was still too fast to observe individual bubbles and droplets (ESI† S2). Again, this suggested that the velocities in the channel were extremely high, potentially in the super-sonic range.

### Nanoparticle sizing and stability

Suspensions of PFC nanoparticles generated in the microfluidic device as described above were measured using a combination of methods. For bubbles of diameter  $1 \mu\text{m}$  and upwards optical counting (Fig. 2b) and electrical conductance (qNano) methods showed good agreement in estimating both bubble size and concentrations. Concentrations were typically of the order of  $10^8$  bubbles per mL. The region of the histogram, in Fig. 2b, defined by the green box corresponds to the range of nanoparticles sizes whose diameter was below the resolution capabilities of the optical microscope. In this regime the particle size/concentration was determined both electrically using the qNano or *via* particle tracking using the NanoSight. The NanoSight data in Fig. 3 indicates a high concentration of particles  $\sim 10^{10} \text{ mL}^{-1}$  for particles of diameter in the range 100–300 nm (the qNano data indicated particle concentrations up to  $10^{12}$  particles per mL).

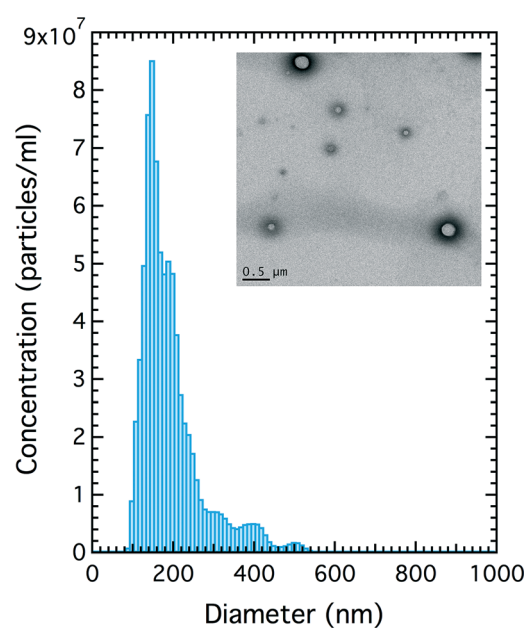
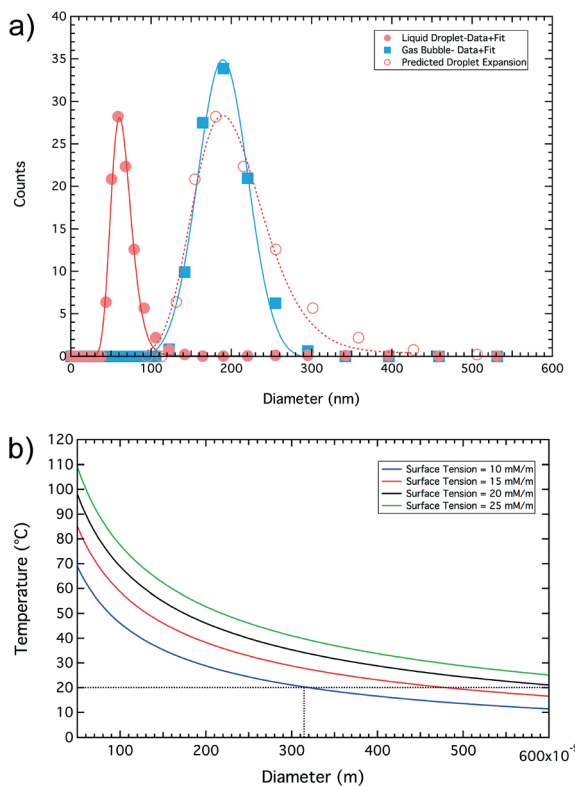


Fig. 3 Particle size of nanoparticles of  $\text{C}_4\text{F}_{10}$  as determined by particle tracking. Inset: TEM image of nanoparticles of  $\text{C}_4\text{F}_{10}$ .

Fig. 4a shows the phase change behavior measured using the Zetasizer as a function of temperature. Particle size was measured in  $\sim 10$  °C steps, for temperatures below 45 °C the nanoparticles were in a liquid state and the size profile did not alter as a function of temperature. The solid circles in Fig. 4a is the average distribution profile for all data obtained below 45 °C. On heating above 57 °C the droplets phase-changed in to a gaseous state (solid squares). Fig. 4b shows the dependence of phase-change temperature for  $\text{C}_4\text{F}_{10}$  as a function of droplet diameter for different surface tensions. The phase change temperature observed in our system (*i.e.*  $<60$  °C) would therefore suggest that the surface tension of our droplets is low and probably between 10 and 15 mN m<sup>-1</sup>. The difference in size observed between data from the NanoSight (Fig. 3) and initial size measurements on the DLS (Fig. 4a) are likely to be due to changes in the sample over time. The same sample was used for both measurements, but the DLS was run two hours after the NanoSight in which the sample was left standing at room temperature. It is likely that some of the larger gas filled particles picked up by the NanoSight have shrunk and condensed to liquid phase  $\text{C}_4\text{F}_{10}$  before being run on the DLS. In addition, some of the larger bubbles will have risen from the bottom of the tube where the sample was taken from. The sample was not agitated in



**Fig. 4** Nanodroplets undergoing thermally induced phase change to gas bubbles. (a) Shows the initial droplet size-distribution (solid red circles), the predicted profile following phase conversion (hollow red circles) and the experimentally determined bubble size post phase conversion (solid blue squares). (b) Shows the calculated phase change temperature, for  $\text{C}_4\text{F}_{10}$ , as a function of droplet size for different droplet surface tensions.

this time to avoid any microbubbles that had risen to the top being mixed back into the sample.

Such low surface tensions would lead to droplets larger than 315 nm being in the gaseous phase whilst smaller ones would remain as liquid droplets. Based on an estimated surface tension of 10 mN m<sup>-1</sup> we can calculate the predicted distribution of bubble sizes, from the initial droplet size distribution, the hollow squares in Fig. 4a was calculated based on the model developed to estimate the “Expansion Ratio” using the approach of Evans *et al.*<sup>42</sup> The “Expansion Ratio” data are provided in the supplementary material (ESI† S4).

A control lipid solution, of the same lipid concentration as used for bubble formation that had been pumped through the tubing, but not the microfluidic device was analysed on the NanoSight. Vesicles in the lipid solution had a much broader size range and lower concentration as particle than after nanobubble/droplet formation in the fluidic device (ESI† S5).

The time dependent behaviour of the particles in terms of size and concentration were also investigated on the qNano. Samples of subnatant collected after separation were kept in the fridge (4 °C) for a period of 17 days and measured on the qNano at different time intervals. Fig. 5 shows the average particle diameter (red axis) and particle concentration (black axis) over time. The data shows that the particles remained stable over the 17 day period with little change in particle diameter or concentration, remaining at  $\sim 260$  nm in diameter and  $4 \times 10^{11}$  particles per mL, respectively. The particles were only measured on the 200 nm pore as this covered the greatest range of particle sizes within the range of interest compared to other pores (100–400 nm).

### Ultrasound measurements

Due to the acoustic impedance mismatch between bubbles and the surrounding liquid we would expect to distinguish between sub-micron sized bubbles and particles, such as liposomes, by measuring the US backscatter from the samples. We would also expect any small particles containing a liquid

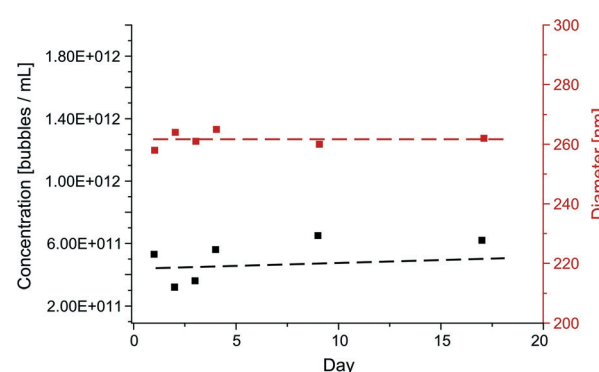


**Fig. 5** Stability testing of nanoparticles measured on the 200 nm pore on the qNano. Nanoparticles kept in the fridge at 4 °C showed excellent size (red) and concentration (black) stability over a 17 day period.



$\text{C}_4\text{F}_{10}$  core to phase change during exposure to the ultrasound field.<sup>23</sup> Suspensions of bubbles and nanoparticles were generated in the microfluidic device as described above. Fig. 6A shows the backscattered US signal from solutions of filtered water containing a concentration of  $2 \times 10^6$  particles per mL of either liposomes or nanoparticles. The scattering signal was corrected for the response of the 15 MHz ultrasound transducer used for this study. In addition, only data acquired within the measured 6 dB bandwidth of the transducer is displayed. The PFC filled nanoparticles showed between a 15–20 dB increase in backscattered signal over equivalent size and concentration of water filled liposomes.

Calculation of the ultrasound response as a function of bubble size (after phase change) predicts that as bubble diameter decreases below 1  $\mu\text{m}$ , the resonant frequency of the bubble increases dramatically >15 MHz (ESI† S6). Fig. 6B

shows the expected resonant frequency response of the nanobubbles used in these experiments, based on their size distribution. Shell parameters for the commonly used phospholipid ultrasound contrast agents, SonoVue and Definity were used for this calculation. This indicates that the nanobubble populations generated in this study would have a theoretical peak resonant frequency at ~60 MHz, but with a range between 15 to >100 MHz which is supportive of the observations made in the backscatter measurements shown in Fig. 6A, where the backscatter of the nanobubbles increases at higher frequencies. This also suggests that the nanobubbles would give even greater backscatter at frequencies higher than the transducer used in these experiments. Many pre-clinical US imaging systems use high frequency transducers in the range 40 to 80 MHz (ref. 43–46) with recent advances to 100 MHz,<sup>47,48</sup> which may be indicative that the nanobubbles will show enhanced contrast and be useful as higher resolution image contrast agents for preclinical imaging and high frequency clinical imaging.

### In vivo characterisation

The *in vivo* behaviour of the nanoparticle samples was investigated in mouse aorta models using the VisualSonics Vevo 770 pre-clinical imaging system with a 40 MHz transducer.

Three CD1 nude mice were imaged using HFUS as described above, each with a different preparation of bubbles or particles; either a raw population of microfluidic bubbles (containing both microbubbles and nanoparticles), or microbubbles or nanoparticles isolated by buoyancy separation. The HFUS images were false coloured (in green) in order to display the change in contrast when the bubble populations were introduced into the vascular system (Fig. 7). A basic comparison between the maximum contrast intensity achieved with each bubble preparation, was done, with the peak intensity from the wash-in curve determined. The peak intensity from the mixed bubble/particle population (Fig. 7(a)) and the nanoparticles population (Fig. 7(b)) were very similar (288 and 296 arbitrary units (A.U.), respectively), and both were much greater than the microbubble only population (Fig. 7(c)) (97 A.U.). These data suggest that the majority of signal seen (with the VisualSonics Vevo 770 40 MHz system) in the mixed bubble/particle population is attributable to the nanoparticle component, with a much lower proportion of the signal coming from microbubbles. Time *vs.* intensity curves (TIC) for the different samples were also taken, the microbubble only sample (from the separated mix) and nanoparticle only sample (from the separated mix) has been added to the ESI† (S7). From the TIC curves, the longevity of the nanoparticle sample compared to the microbubble only sample can clearly be seen, with contrast intensity at >131 lasting 40 s post injection. This was also comparable to the whole mixed population of microbubbles and nanoparticles, which showed a contrast intensity of over 100 for the 40 s post injection, suggesting at these higher frequencies much of the contrast signal observed was from the

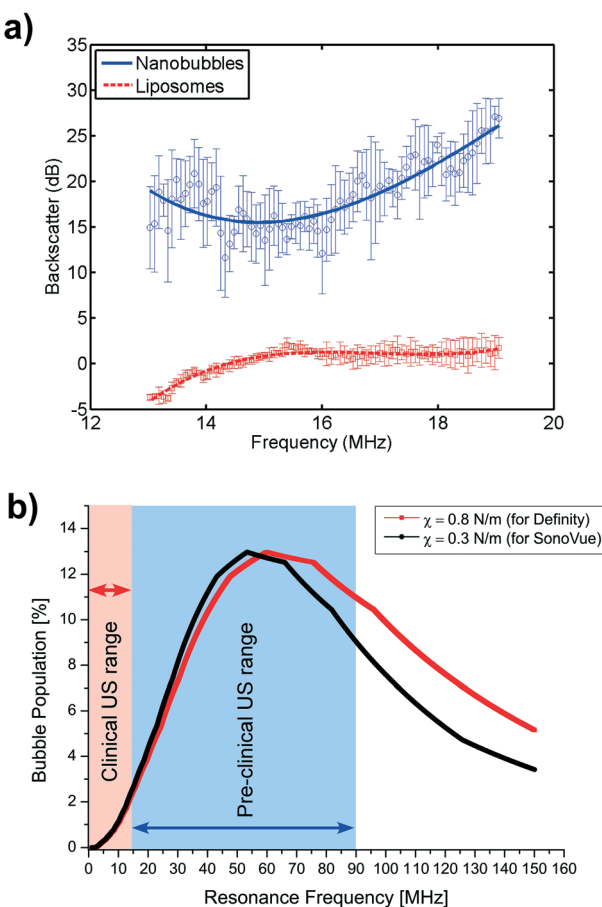
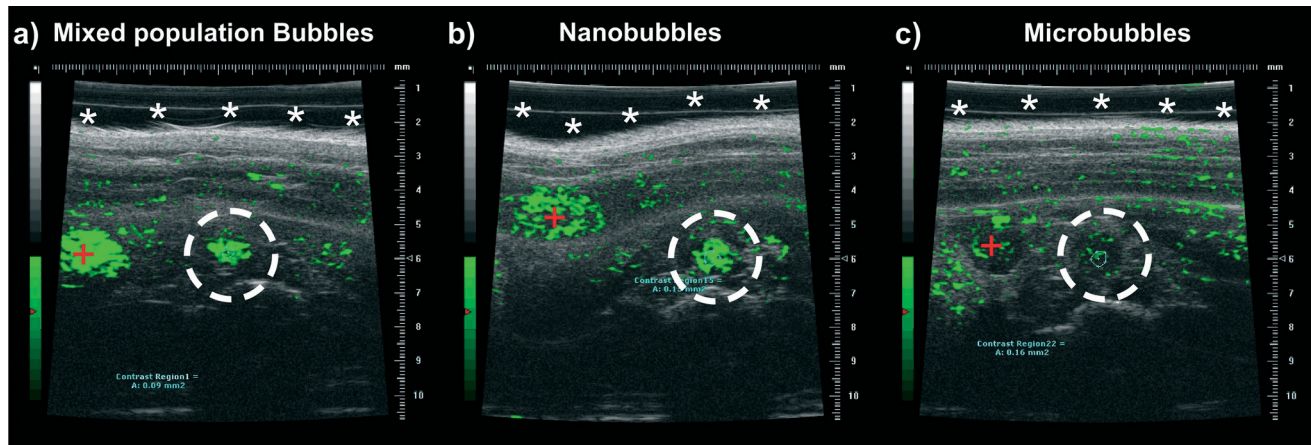


Fig. 6 (a) Ultrasound backscatter signal of nanoparticles and liposomes. Over the 6 dB bandwidth of the ultrasound transducer the nanobubbles showed between a 15–20 dB increase in signal over an equivalent size and concentration of liposomes. A 15 MHz transducer was used in conjunction with a pulser/receiver to transmit a broadband ultrasound signal and detect the backscatter. Error bars represent the standard deviation of the measured backscatter for three repeat samples. (b) Distribution of calculated resonance frequencies for a population of nanobubbles – showing a peak resonant frequency of ~55 MHz. The plot shows the US frequency ranges for both clinical and pre-clinical imaging.





**Fig. 7** HFUS images of mouse aorta after bolus delivery of bubble agents. A bubble preparation was delivered via tail vein catheter at  $0.6 \text{ ml min}^{-1}$  regulated by a syringe driver. (a. Mixed population bubbles b. nanobubbles c. microbubbles). The aorta was identified in each mouse (circled) and the wash-in data for the aorta were exported to GraphPad Prism (version 6.05 for Windows, GraphPad Software, La Jolla, California, USA) to determine the peak wash-in intensity for each bubble population (288 A.U. 296 A.U. and 97 A.U. for the mixed, nanobubble and microbubble populations, respectively).

nanoparticle fraction. The high contrast intensity observed from mixed bubble and nanoparticle only samples in *in vivo* experiments could be attributed to two factors. The first being that a higher frequency transducer (40 MHz) was used for these experiments, which is much closer to the expected resonant frequency of the sub-micron bubbles (60 MHz) than the 15 MHz transducer used in the phantom experiments. In addition, ultrasound activated phase change; the elevated temperature of *in vivo* experiments is likely to facilitate the phase conversion of smaller fluid filled  $\text{C}_4\text{F}_{10}$  droplets into gaseous nanobubbles, enhancing the contrast signal.

## Conclusions

We have demonstrated the first microfluidic preparation of high concentrations of nanoparticles of  $\text{C}_4\text{F}_{10}$  using a micro-spray flow regime. Nanoparticles with diameters between 50 nm and 1  $\mu\text{m}$  were produced at high concentration, of the order  $10^{11}$ – $10^{12}$  nanoparticles per mL, as counted and sized by qNano, and of which  $\sim 10^{10}$   $\text{mL}^{-1}$  were fluorocarbon droplets. Nanoparticle populations were likely to be mix of liquid and gaseous cores of  $\text{C}_4\text{F}_{10}$  for diameters  $< 1 \mu\text{m}$ . Ultrasound measurements confirmed the presence of gas filled particles that showed higher backscatter signal than water filled liposomes of a similar size. Nanoparticles imaged in mice aorta showed excellent contrast intensity when compared to samples of mixed bubble sizes (micro- and nano-) and microbubbles only, suggesting that at high frequencies used in pre-clinical imaging, nanoparticles contribute highly to the contrast intensity observed in US imaging. These nanoparticles have the potential to provide higher resolution contrast imaging when working at higher ultrasound frequencies. Further, their ability to perfuse into tumours would provide better resolution in diagnostic ultrasound and increase efficiency of bubble based drug delivery systems. Future work will include

tailoring the microspray regime to preferentially produce nanoparticles over micron sized bubbles by optimising flow and gas pressures and bubble shell chemistry. Nanoparticles will also be investigated for improved extra-cellular imaging in tumours and drug delivery potential in *in vitro* and *in vivo* models.

## Acknowledgements

We gratefully acknowledge financial sponsorship from the EPSRC (EP/K023845/1). J. M. would like to acknowledge support from an early career Leverhulme fellowship (ECF-2013-247). We also thank the Leeds Microbubble Consortium for valued discussions.

## References

1. D. Cosgrove, *Eur. J. Radiol.*, 2006, **60**, 324–330.
2. R. H. Abou-Saleh, S. A. Peyman, K. Critchley, S. D. Evans and N. H. Thomson, *Langmuir*, 2013, **29**, 4096–4103.
3. S. Sirsi and M. Borden, *Bubble Sci. Eng. Technol.*, 2009, **1**, 3–17.
4. A. Alzaraa, G. Gravante, W. Y. Chung, D. Al-Leswas, M. Bruno, A. R. Dennison and D. M. Lloyd, *Am. J. Surg.*, 2012, **204**, 355–366.
5. J. McLaughlan, N. Ingram, P. R. Smith, S. Harput, P. L. Coletta, S. Evans and S. Freear, *IEEE Trans. Ultrason. Ferroelectr. Freq. Control*, 2013, **60**, 2511–2520.
6. K. Kooiman, H. J. Vos, M. Versluis and N. de Jong, *Adv. Drug Delivery Rev.*, 2014, **72**, 28–48.
7. M. J. K. Blomley, J. C. Cooke, E. C. Unger, M. J. Monaghan and D. O. Cosgrove, *Br. Med. J.*, 2001, **322**, 1222–1225.
8. W. B. Zimmerman, V. Tesar and H. C. H. Bandulasena, *Curr. Opin. Colloid Interface Sci.*, 2011, **16**, 350–356.
9. A. Agarwal, W. J. Ng and Y. Liu, *Chemosphere*, 2011, **84**, 1175–1180.



10 F. Y. Ushikubo, T. Furukawa, R. Nakagawa, M. Enari, Y. Makino, Y. Kawagoe, T. Shiina and S. Oshita, *Colloids Surf., A*, 2010, **361**, 31–37.

11 K. Ohgaki, N. Q. Khanh, Y. Joden, A. Tsuji and T. Nakagawa, *Chem. Eng. Sci.*, 2010, **65**, 1296–1300.

12 S. Ljunggren and J. C. Eriksson, *Colloids Surf., A*, 1997, **129**, 151–155.

13 Z. Xing, J. Wang, H. Ke, B. Zhao, X. Yue, Z. Dai and J. Liu, *Nanotechnology*, 2010, **21**.

14 H. Wu, N. G. Rognin, T. M. Krupka, L. Solorio, H. Yoshiara, G. Guenette, C. Sanders, N. Kamiyama and A. A. Exner, *Ultrasound Med. Biol.*, 2013, **39**, 2137–2146.

15 H.-P. Tong, L.-F. Wang, Y.-L. Guo, L. Li, X.-Z. Fan, J. Ding and H.-Y. Huang, *Ultrasound Med. Biol.*, 2013, **39**, 2147–2157.

16 Y. Wang, X. Li, Y. Zhou, P. Huang and Y. Xu, *Int. J. Pharm.*, 2010, **384**, 148–153.

17 X. Zhang, Y. Zheng, Z. Wang, S. Huang, Y. Chen, W. Jiang, H. Zhang, M. Ding, Q. Li, X. Xiao, X. Luo, Z. Wang and H. Qi, *Biomaterials*, 2014, **35**, 5148–5161.

18 R. Cavalli, A. Bisazza, M. Trott, M. Argenziano, A. Civra, M. Donalisio and D. Lembo, *Int. J. Nanomed.*, 2012, **7**, 3309–3318.

19 M. A. Wheatley, F. Forsberg, N. Dube, M. Patel and B. E. Oeffinger, *Ultrasound Med. Biol.*, 2006, **32**, 83–93.

20 D. S. Wagner, N. A. Delk, E. Y. Lukianova-Hleb, J. H. Hafner, M. C. Farach-Carson and D. O. Lapotko, *Biomaterials*, 2010, **31**, 7567–7574.

21 L. J. E. Anderson, E. Hansen, E. Y. Lukianova-Hleb, J. H. Hafner and D. O. Lapotko, *J. Controlled Release*, 2010, **144**, 151–158.

22 C.-H. Wang, Y.-F. Huang and C.-K. Yeh, *Langmuir*, 2011, **27**, 6971–6976.

23 P. S. Sheeran and P. A. Dayton, *Curr. Pharm. Des.*, 2012, **18**, 2152–2165.

24 T. O. Matsunaga, P. S. Sheeran, S. Luo, J. E. Streeter, L. B. Mullin, B. Banerjee and P. A. Dayton, *Theranostics*, 2012, **2**, 1185–1198.

25 P. S. Sheeran, J. E. Streeter, L. B. Mullin, T. O. Matsunaga and P. A. Dayton, *Ultrasound Med. Biol.*, 2013, **39**, 893–902.

26 P. S. Sheeran, J. D. Rojas, C. Puett, J. Hjelmquist, C. B. Arena and P. A. Dayton, *Ultrasound Med. Biol.*, 2015, **41**, 814–831.

27 P. S. Sheeran, V. P. Wong, S. Luo, R. J. McFarland, W. D. Ross, S. Feingold, T. O. Matsunaga and P. A. Dayton, *Ultrasound Med. Biol.*, 2011, **37**, 1518–1530.

28 M. Hashimoto and G. M. Whitesides, *Small*, 2010, **6**, 1051–1059.

29 E. Castro-Hernandez, W. van Hoeve, D. Lohse and J. M. Gordillo, *Lab Chip*, 2011, **11**, 2023–2029.

30 M. Hashimoto, S. S. Shevkoplyas, B. Zasonska, T. Szymborski, P. Garstecki and G. M. Whitesides, *Small*, 2008, **4**, 1795–1805.

31 K. Hettiarachchi, E. Talu, M. L. Longo, P. A. Dayton and A. P. Lee, *Lab Chip*, 2007, **7**, 463–468.

32 E. Talu, K. Hettiarachchi, R. L. Powell, A. P. Lee, P. A. Dayton and M. L. Longo, *Langmuir*, 2008, **24**, 1745–1749.

33 T. D. Martz, P. S. Sheeran, D. Bardin, A. P. Lee and P. A. Dayton, *Ultrasound Med. Biol.*, 2011, **37**, 1952–1957.

34 S. A. Peyman, R. H. Abou-Saleh, J. R. McLaughlan, N. Ingram, B. R. G. Johnson, K. Critchley, S. Freear, J. A. Evans, A. F. Markham, P. L. Coletta and S. D. Evans, *Lab Chip*, 2012, **12**, 4544–4552.

35 N. Maennicke, M. Schoene, M. Gottwald, F. Goebel, M. L. Oelze and K. Raum, *Ultrasound Med. Biol.*, 2014, **40**, 244–257.

36 C. P. Pavlovich, T. C. Cornish, J. K. Mullins, J. Fradin, L. Z. Mettee, J. T. Connor, A. C. Reese, F. B. Askin, R. Luck, J. I. Epstein and H. B. Burke, *Urol. Oncol.*, 2014, **32**, 34.e27–34.e32.

37 E. Ruckenstein, *Colloids Surf., A*, 2013, **423**, 112–114.

38 J. M. Gorce, M. Ardit and M. Schneider, *Invest. Radiol.*, 2000, **35**, 661–671.

39 R. E. Apfel and C. K. Holland, *Ultrasound Med. Biol.*, 1991, **17**, 179–185.

40 C. C. Church, *Acoust. Res. Lett. Online*, 2005, **6**, 162–168.

41 K. Chen and H. J. Richter, *Int. J. Multiphase Flow*, 1997, **23**, 699–712.

42 D. R. Evans, D. F. Parsons and V. S. J. Craig, *Langmuir*, 2006, **22**, 9538–9545.

43 A. Needles, D. E. Goertz, R. Karshafian, E. Cherin, A. S. Brown, P. N. Burns and F. S. Foster, *Ultrasound Med. Biol.*, 2008, **34**, 1139–1151.

44 A. Needles, M. Ardit, N. G. Rognin, J. Mehi, T. Coulthard, C. Bilan-Tracey, E. Gaud, P. Frinking, D. Hirson and F. S. Foster, *Ultrasound Med. Biol.*, 2010, **36**, 2097–2106.

45 J. McLaughlan, N. Ingram, R. Abou-Saleh, S. Harput, T. Evans, S. Evans, L. Coletta, S. Freear and Ieee, *IEEE Int. Ultrason. Symp.*, 2013, 1493–1496.

46 C. Sun, V. Sboros, M. B. Butler and C. M. Moran, *Ultrasound Med. Biol.*, 2014, **40**, 541–550.

47 J. Mamou, O. Aristizabal, R. H. Silverman, J. A. Ketterling and D. H. Turnbull, *Ultrasound Med. Biol.*, 2009, **35**, 1198–1208.

48 H. Choi, H.-C. Yang and K. K. Shung, *Ultrasonics*, 2014, **54**, 754–758.

